



INSTITUT DE FRANCE
Académie des sciences

Comptes Rendus

Mécanique


Safa Boudhraa, Alfonso Fernandez del Rincon, Fakher Chaari,
Mohamed Haddar and Fernando Viadero

**Tooth defect detection in planetary gears by the current signature
analysis: numerical modelling and experimental measurements**

Volume 349, issue 2 (2021), p. 275-298

<<https://doi.org/10.5802/crmeca.84>>

© Académie des sciences, Paris and the authors, 2021.
Some rights reserved.

 This article is licensed under the
CREATIVE COMMONS ATTRIBUTION 4.0 INTERNATIONAL LICENSE.
<http://creativecommons.org/licenses/by/4.0/>



*Les Comptes Rendus. Mécanique sont membres du
Centre Mersenne pour l'édition scientifique ouverte*
www.centre-mersenne.org



Short paper / Note

Tooth defect detection in planetary gears by the current signature analysis: numerical modelling and experimental measurements

Safa Boudhraa^{ⓐ, ⓑ}, Alfonso Fernandez del Rincon[ⓐ], Fakher Chaari^{ⓐ*, ⓑ},
Mohamed Haddar^{ⓐ ⓑ} and Fernando Viadero[ⓐ]

^a Department of Structural and Mechanical Engineering, Faculty of Industrial and Telecommunications Engineering, University of Cantabria, Avda de los Castros s/n 39005, Santander, Spain

^b Laboratory of Mechanics, Modelling and Production (LA2MP), National School of Engineers of Sfax, BP1173, 3038 Sfax, Tunisia

E-mails: Safa.boudhraa@alumnos.unican.es (S. Boudhraa), alfonso.fernandez@unican.es (A. Fernandez del Rincon), fakher.chaari@gmail.com (F. Chaari), mohamed.haddar@enis.rnu.tn (M. Haddar), fernando.viadero@unican.es (F. Viadero)

Abstract. Monitoring transmission systems is a huge scientific focus to prevent any anomaly and malfunctioning damaging the system. Several methods were used to investigate the gears behaviour and mainly its state. And until the last century, vibrations signals were the most performing technique in this field. However, nowadays, other alternatives are considered more accurate and accessible such as controlling the motor current signals to study the behaviour of the mechanical system. Within this context, this paper aims to study the electromechanical interaction between a double stage of planetary gearboxes driven by an asynchronous machine. The model used is based on a Park transformation for modelling the asynchronous machine and a torsional model to describe the dynamic behaviour of the double-stage planetary gearbox. Through this approach, the numerical simulations illustrate the impact of the tooth gear defect on the signature of the motor current. The results obtained from the simulations will be presented in the time domain and the frequency domain using the fast Fourier transform and the Hanning window to highlight the mechanical frequencies in the phase current spectrum. This work will be distinguished by validating the numerical results using experimental measurements, which will be displayed in order to justify the sensitivity of the model developed.

Keywords. Asynchronous motor, Experimental measurements, Gears defects, Motor current, Park transformation, Planetary gears.

Manuscript received 22nd March 2021, revised 21st April 2021, accepted 28th April 2021.

* Corresponding author.

1. Introduction

Planetary gearboxes have been used in different industrial domains especially in applications that recommend large torque transmission. Due to its spatial configuration, planetary transmissions are complicated to model, but the importance of these gear systems in aerospace and energy generation applications makes the effort worth it. Despite its enormous use, durability and condition monitoring of these systems are still a major scientific trend also an industrial focus. Gears are exposed to several types of defects. Those defects are divided into two main families as stated in Chaari *et al.* [1]; geometry defects, which concerns manufacturing and assembly defects, and teeth defects, that attack the system, like pitting, cracks, or breakages, etc. Thus, many researchers had worked on evaluating gears state by different techniques based on nondestructive tests that aim to provide early detection of any anomalies in the system. Until the beginning of the last century, studying the vibration signals of the rotating machinery has been the most performing tool to evaluate the dynamic behaviour and to detect the presence of any mechanical defect.

In order to study the dynamic behaviour of these gears in the presence of tooth pitting and cracking, Chaari *et al.* [2], had worked on modelling defected planetary gearboxes. Likewise, Fernandez *et al.* [3, 4] had developed a model that studies the interaction between different pairs of teeth in contact. Li *et al.* [5] had used an extraction method using both the Empirical Mode Decomposition and Autocorrelation Local Cepstrum to detect fault diagnosis of sophisticated multistage gearbox.

The impact of tooth defect generates a torque variation which is manifested in a significant modification of contact ratio. Within the same context, Qinkai *et al.* [6] had also investigated the localization of tooth breakage on a wind turbine planetary gear system, considering the manufacturing errors. Indeed, the severity of the impact depends on the type, placement, and size of the defect. Therefore, each defect has different signature that will lead to detect and identify it by analysing the output signals. The tooth defect is characterized in the vibration signal by its key frequency. Through the frequency spectrum, the vibration signals of a single-stage planetary gearbox provide an overview of the teeth defect. This correlation is identified and explained by a numerical model and experimental investigations developed by Qiang and Qinghua [7]. Moreover, vibration signals have been the key of diagnosing the gears state in helicopters, not only in detecting gears defects but also in studying its impact on the behaviour of the system and its natural frequencies [8–10].

However, the use of this technique has several limitations, such as the sensitivity of the sensors used to the operating conditions. These sensors used can enhance the appearance of significant noise in the signals due to perturbations. Also, for complicated rotating machineries it is very difficult to get access to implement the sensors. Therefore, the industry is interested in a more accurate technique that provides a global overview about the system behaviour with least cost. In this framework, innovative engineering is oriented to the multi-domain interaction that aims to control the mechanical systems by involving different physical phenomena, such as the motor current signature analysis (MCSA), which has been one of the most used techniques in this field.

And so forth, Kar *et al.* [11] had worked on investigating other techniques to early defects detection. The paper was based on a comparative study between vibrations and motor current intensity in the presence of tooth defect. The MCSA was used also to evaluate the influence of the electromagnetic effect on the natural vibration characteristics of the gearbox in the work of Yi *et al.* [12].

Investigating the motor's behaviour was used in several studies to monitor the mechanical system, detecting defects. This Proposal was highlighted by the work developed by Balan *et al.* [13] studying the impact of the unbalance seen in the motor's component on the motor current signal.

The use of the current signal to investigate the gearbox state is considered more accurate given the accessibility for different operating conditions and complex systems. This is one additional advantage comparing with the vibration signals, since in the stator current, the modulations produced by the planet motion do not appear [14], which makes the spectrum more significant. Different research papers [14, 15] had proved the sensitivity of this method not only to detect the state of the system but also to localize and identify the defect. Nandi *et al.* [16, 17] had used the motor current signal analysis MCSA to show that the appearance of the static and dynamic air gap eccentricity simultaneously is seen in the amplitude modulation of the stator current. Kia [18] had develop the idea of using the current of the driving machine to detect a mechanical system defect. In fact, this development is based on a fundamental study of the effect of the torsional vibration for two mass–spring systems in the stator current signal [19, 20]. It had showed that for two different joints inertia–mass systems, the source of torque oscillation is related to a single torsional vibrations frequency.

For the electrical part, the modelling of the asynchronous machine was done in different studies by various approaches such as analytical, semi-analytical, or finite element modelling. The choice of the approach depends on whether the need of it or mainly the operating conditions which define the hypothesis of modelling. One of the basic method used in the analytical modelling is the Park transformation [21], that transforms a tri-phased motor, to an equivalent two-phase machine called a d - q model. Even though finite element methods are the most used nowadays for simple problems and controlling the electrical machines, the Park transformation is recommended for rapidly resolving situations in steady state operating conditions. Few researchers worked on the planetary gears monitoring using the MSCA, Ottewill *et al.* [22] had investigated the impact of the tooth defect in epicyclic gearboxes on the current signals using numerical modelling pursued by experimental validation.

The importance of using the motor current signature analysis is highlighted mainly in the accessibility to the information through the driving system. Electric machine current signal analysis provides an alternative technique for planetary gearbox fault diagnosis. The faults generated in the mechanical system led to changes in electric current intensity because of mechanical–magnetic–electric interactions, and hence electric current signals contain rich information about planetary gearbox health conditions. Goa had demonstrated [23] that the impact of a gear defect is sidebands of the supply frequency of the motor. Planetary gearbox faults result in input torque oscillations, leading to both amplitude modulation and frequency modulation (AM–FM) effects on stator current signals.

Besides the accessibility, this technique is mainly used in power stations to avoid system damage. Also, online fault monitoring can be done without shutdown the motor [24].

The study presented in this paper extends the approach of studying the electromechanical interaction's ability to monitor the mechanical system. This work is going to be structured in the paper as follows. Section 2 is dedicated to the theoretical development of an electromechanical system composed of a planetary gearbox and an induction motor. In Section 3, the experimental testbench is described, composed of a Siemens induction motor and a back-to-back planetary gearbox. In Section 4, the numerical model developed in Section 2 will be adopted to simulate the experimental rig. Finally, the last section highlights the accuracy of the current signals in investigating the state of the gears in a double-stage planetary gearbox. And later, experimental measurements were taken in order to validate the sensitivity of the model. The real contribution in this work is justifying the numerical approach by experiments. Lastly, some conclusions are presented.

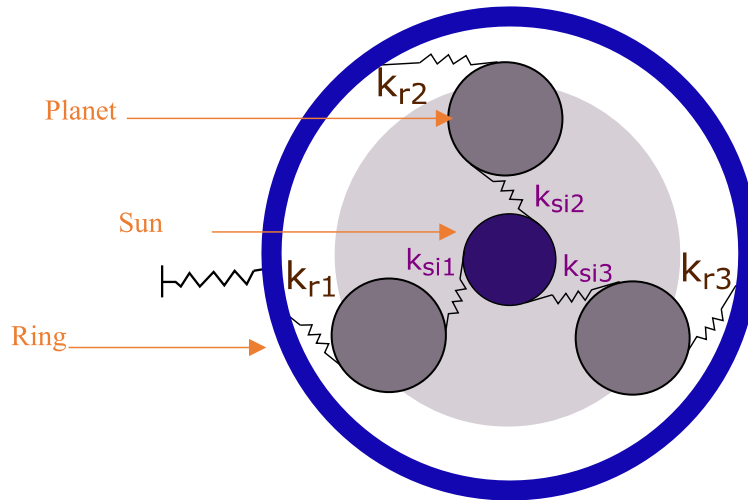


Figure 1. A torsional model of a double-stage planetary gearbox.

2. Theoretical formulation

The electromechanical model is composed of three parts:

Starting from the mechanical model of planetary gears, this model is based mainly on the motion expression that illustrates the dynamic behaviour of the system, considering only the torsional degree of freedom. The second part will be devoted to the model of the asynchronous motor using the Park transformation that aims to transfer the three-phased motor to an equivalent circuit. Finally, in the last part, a global electromechanical system based on both previous models is presented. The coupling terms between the electrical part and the mechanical system are due to the electromechanical torque coming from the motor and the vibration's responses of the gearboxes to the motor.

2.1. Mechanical model

The mechanical system developed in this study is a planetary gear set. In order to simplify the model, only torsional degrees of freedom were considered, and therefore only the torsional stiffness will be involved in the model, Figure 1. Modelling the planetary gears used is based on the development of Lin and Parker [25] and its dynamic model. So, the model seen in Figure 1 presents $(n + 3)$ degrees of freedom each gearbox, where n is the planets number (given 3 in this case).

The equation of motion for the mechanical system is expressed as follows:

$$M\ddot{q} + C\dot{q} + (K(t) + K_c)q = F(t), \quad (1)$$

where $F(t)$ and $q(t)$ are external force and displacement vector, respectively. M represents the diagonal mass matrix

$$M = \text{diag}(m_c + Nm_p, m_r, m_s, m_1, m_2, m_3) \quad (2)$$

and $m_i = I_i / r_i$, where I_i refers to the inertia of each component and r_i is the base radius of the component i . Finally, C refers to the damping matrix, taken as a Rayleigh damping.

The mesh stiffness of the system is given by the matrix both $K(t)$ (3).

In each set of gears, the sun and the ring were connected to the three planets via the mesh stiffness given by K_{inj} , K_{ij} , where $i \in \{s, r\}$, where s refers to the sun and r to the ring, $n \in \{t, r\}$

(*r* refers to the reaction gearbox, *t* refers to test gearbox) and *j* presents the number of planets, $j \in \{1, 2, 3\}$. The mesh stiffness is usually assumed as one linear spring as seen in Figure 1, acting on the line of action. Thus, the possibility of considering one stiffness for each contact [26].

$$K(t) = \begin{bmatrix} \sum_{i=1}^3 (K_{si}(t) + K_{ri}(t)) - \sum_{i=1}^3 K_{ri}(t) - \sum_{i=1}^3 K_{ri}(t) & K_{r1}(t) - K_{s1}(t) & K_{r2}(t) - K_{s2}(t) & K_{r3}(t) - K_{s3}(t) \\ -\sum_{i=1}^3 K_{ri}(t) & \sum_{i=1}^3 K_{ri}(t) & 0 & -K_{r1}(t) & -K_{r2}(t) & -K_{r3}(t) \\ -\sum_{i=1}^3 K_{si}(t) & 0 & \sum_{i=1}^3 K_{si}(t) & K_{s1}(t) & K_{s2}(t) & K_{s3}(t) \\ K_{r1}(t) - K_{s1}(t) & -K_{s3}(t) & K_{s1}(t) & K_{s1}(t) + K_{r1}(t) & 0 & 0 \\ K_{r2}(t) - K_{s2}(t) & -K_{r2}(t) & K_{s2}(t) & 0 & K_{s2}(t) + K_{r2}(t) & 0 \\ K_{r3}(t) - K_{s3}(t) & -K_{r3}(t) & K_{s3}(t) & 0 & 0 & K_{s3}(t) + K_{r3}(t) \end{bmatrix}. \tag{3}$$

2.2. Electrical model

Modelling the electrical machine has been a tool whether to study the machine state or to ensure the physical coupling between motor and any mechanical systems. The model used depends on the application [27]. Thus, the objective of this study is to investigate the state of the mechanical system. For this reason, it was decided to work with a Park transformation since it is an analytical approach with settings easily identifiable [28]. Park transformation is an analytical method that aims to transform a three-phased machine into a bi-directional, maintaining the physical phenomena. Since this method recommends theoretical developments of equations describing the electromagnetic response of an asynchronous motor, it is necessary to make the following assumptions to simplify the complexity of the system.

- The saturation is neglected: the own and mutual inductances are independent of the currents flowing in the different windings.
- Hysteresis and eddy currents are not considered in the magnetic parts because it is assumed that the magnetic circuit is perfectly laminated.
- The notches are supposed to be infinitely thin in order to neglect the notches effect.
- Magnetomotive forces are sinusoidally distributed in the air gap and are assumed uniform; there is symmetry with respect to the magnetic axis of the windings.

The choice of the *dq0* framework related to the rotating system depends on the objective of the study [29]. The change from a three-phased machine to a bi-phased was ensured by the matrix.

$$T_{dq0} = \sqrt{\frac{2}{3}} \begin{bmatrix} \cos\theta & \cos\left(\theta - \frac{2\pi}{3}\right) & \cos\left(\theta + \frac{2\pi}{3}\right) \\ -\sin(\theta) & -\sin\left(\theta - \frac{2\pi}{3}\right) & -\sin\left(\theta + \frac{2\pi}{3}\right) \\ \frac{1}{\sqrt{2}} & \frac{1}{\sqrt{2}} & \frac{1}{\sqrt{2}} \end{bmatrix}, \tag{4}$$

where $\omega = d\theta/dt$.

The relation ensuring the interaction between the magnetic field and the electric circuit is given by the Law of Faraday.

$$v_{ij} = R_j i_{ij} + \frac{d\psi_{ij}}{dt}, \tag{5}$$

where R_j : resistance of *j* phase; *j*: stator, rotor; *i*: coiling (a, b, c).

ψ_{ij} : the magnetic flux of *j* phase.

i_{ij} : the current of the *j* phase.

The asynchronous motor case is squirrel cage motor, which explains the following expression

$$v_{ar} = v_{br} = v_{cr} = 0. \tag{6}$$

The relations between the magnetic flux ψ and the current in each phase coiling, noted i_{ij} , are presented by the matrix expression below (7) and (8)

$$\begin{Bmatrix} \psi_{as} \\ \psi_{bs} \\ \psi_{cs} \end{Bmatrix} = \begin{bmatrix} L_{as} & M_{as} & M_{rs} \cos \theta & M_{rs} \cos \theta & M_{rs} \cos \left(\theta + \frac{2\pi}{3} \right) & M_{rs} \cos \left(\theta - \frac{2\pi}{3} \right) \\ M_{as} & L_{as} & M_{rs} \cos \theta & M_{rs} \cos \left(\theta - \frac{2\pi}{3} \right) & M_{rs} \cos \theta & M_{rs} \cos \left(\theta + \frac{2\pi}{3} \right) \\ M_{as} & M_{as} & L_{as} & M_{rs} \cos \left(\theta + \frac{2\pi}{3} \right) & M_{rs} \cos \left(\theta + \frac{2\pi}{3} \right) & M_{rs} \cos \theta \end{bmatrix} * \begin{Bmatrix} i_{as} \\ i_{bs} \\ i_{cs} \\ i_{ar} \\ i_{br} \\ i_{cr} \end{Bmatrix} \tag{7}$$

$$\begin{Bmatrix} \psi_{ar} \\ \psi_{br} \\ \psi_{cr} \end{Bmatrix} = \begin{bmatrix} M_{rs} \cos \theta & M_{rs} \cos \left(\theta - \frac{2\pi}{3} \right) & M_{rs} \cos \left(\theta + \frac{2\pi}{3} \right) & L_{ar} & M_{ar} & M_{ar} \\ M_{rs} \cos \left(\theta + \frac{2\pi}{3} \right) & M_{rs} \cos \theta & M_{rs} \cos \left(\theta - \frac{2\pi}{3} \right) & M_{ar} & L_{ar} & M_{ar} \\ M_{rs} \cos \left(\theta - \frac{2\pi}{3} \right) & M_{rs} \cos \left(\theta + \frac{2\pi}{3} \right) & M_{rs} \cos \theta & M_{ar} & M_{ar} & L_{ar} \end{bmatrix} * \begin{Bmatrix} i_{as} \\ i_{bs} \\ i_{cs} \\ i_{ar} \\ i_{br} \\ i_{cr} \end{Bmatrix}, \tag{8}$$

where

M_{as} : mutual inductance between two phases of the stator

M_{ar} : mutual inductance between two phases of the rotor

L_{as} : self-inductance of the stator

L_{ar} : self-inductance of the rotor

M_{rs} : maximum inductance between a stator's phase and a rotor's phase.

The previous electrical and magnetic expressions are described in the same frame dq .

$$\begin{Bmatrix} v_{ds} \\ v_{qs} \end{Bmatrix} = \begin{bmatrix} R_s & 0 \\ 0 & R_s \end{bmatrix} \begin{Bmatrix} i_{ds} \\ i_{qs} \end{Bmatrix} + \frac{d}{dt} \begin{Bmatrix} \psi_{ds} \\ \psi_{qs} \end{Bmatrix} + \begin{bmatrix} 0 & -\omega_e \\ \omega_e & 0 \end{bmatrix} \begin{Bmatrix} \psi_{ds} \\ v_{qs} \end{Bmatrix} \tag{9}$$

$$\begin{Bmatrix} v_{dr} \\ v_{qr} \end{Bmatrix} = \begin{bmatrix} R_r & 0 \\ 0 & R_r \end{bmatrix} \begin{Bmatrix} i_{dr} \\ i_{qr} \end{Bmatrix} + \frac{d}{dt} \begin{Bmatrix} \psi_{dr} \\ \psi_{qr} \end{Bmatrix} + \begin{bmatrix} 0 & -\omega_r \\ \omega_r & 0 \end{bmatrix} \begin{Bmatrix} \psi_{dr} \\ v_{qr} \end{Bmatrix} \tag{10}$$

$$\begin{Bmatrix} \psi_{ds} \\ \psi_{dr} \end{Bmatrix} = \begin{bmatrix} L_s & L_m \\ L_m & L_r \end{bmatrix} \begin{Bmatrix} i_{ds} \\ i_{dr} \end{Bmatrix} \tag{11}$$

$$\begin{Bmatrix} \psi_{qs} \\ \psi_{qr} \end{Bmatrix} = \begin{bmatrix} L_s & L_m \\ L_m & L_r \end{bmatrix} \begin{Bmatrix} i_{qs} \\ i_{qr} \end{Bmatrix}. \tag{12}$$

Supposing $L_s = L_{as} - M_{as}$: stator synchronous inductance

$L_r = L_{ar} - M_{ar}$: rotor synchronous inductance

$L_m = (3/2)M_{rs}$: magnetizing inductance,

where $\omega_s = p\pi f$, $\omega = p\pi N/30$ and $\omega_r = \omega - \omega_s$.

The previous analytical development of the three-phased motor had contributed to give a bi-phased equivalent machine, as presented in Figure 2. The stator current and the rotor magnetic flux, written in the same framework had led to the global asynchronous machine model given by (14).

$$\frac{d}{dt} \{X(t)\} = [A]\{X(t)\} + [B]\{U(t)\}, \tag{13}$$

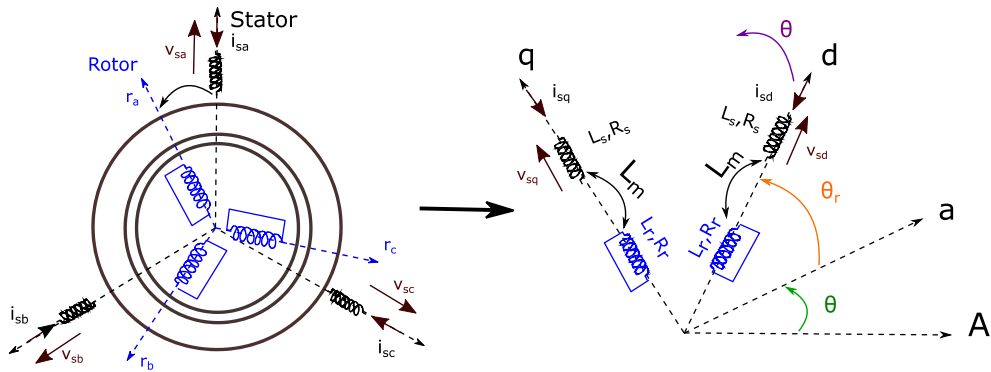


Figure 2. The equivalent bi-phased machine obtained from an asynchronous motor.

Table 1. Motor parameters

Parameters	Value
R_s	9.172 Ω
R_r	5.162 Ω
L_s	0.115 H
L_r	0.0943 H
L_m	0.0943 H

where $X(t)$ the state vector given by

$$X(t) = \{i_{ds} \ i_{qs} \ \psi_{dr} \ \psi_{qr}\}^T \tag{14}$$

$$\Rightarrow \frac{d}{dt} \begin{Bmatrix} i_{ds} \\ i_{qs} \\ \psi_{dr} \\ \psi_{qr} \end{Bmatrix} = \begin{bmatrix} e_{11} & e_{12} * \omega_s & e_{13} & e_{14} * \omega \\ e_{21} * \omega_s & e_{22} & e_{23} * \omega & e_{24} \\ e_{31} & 0 & e_{33} & e_{34} * \omega_r \\ 0 & e_{42} & e_{43} * \omega_r & e_{44} \end{bmatrix} \begin{Bmatrix} i_{ds} \\ i_{qs} \\ \psi_{dr} \\ \psi_{qr} \end{Bmatrix} + \begin{bmatrix} \frac{1}{\sigma L_s} & 0 \\ 0 & \frac{1}{\sigma L_s} \\ 0 & 0 \\ 0 & 0 \end{bmatrix} \begin{Bmatrix} v_{ds} \\ v_{qs} \end{Bmatrix}, \tag{15}$$

where

$$\begin{aligned} \sigma &= 1 - \left(\frac{L_m^2}{L_s L_r}\right); \quad T_r = \frac{L_r}{R_r}; \quad T_s = \frac{L_s}{R_s} \\ e_{11} &= e_{22} = -\left(\frac{1}{\sigma T_s} + \frac{(1-\sigma)}{\sigma T_r}\right), \quad e_{33} = e_{44} = -\frac{1}{T_r} \\ e_{12} &= e_{34} = 1, \quad e_{21} = e_{43} = -1 \\ e_{13} &= e_{24} = \frac{(1-\sigma)}{\sigma T_r L_m}, \quad e_{31} = e_{42} = \frac{L_m}{T_r} \\ e_{14} &= -e_{23} = \frac{(1-\sigma)}{\sigma L_m}. \end{aligned}$$

The electrical parameters of the motor are given in the Table 1. The motor’s parameters mainly used in the simulations (resistance and inductance) were determined by experimental measurements through the starter “MICROMASTER”.

2.3. Electromechanical problem

The combination of all the expressions had led to a global electromechanical system (16). The coupled state variable vector contains different electrical parameters of the motor (current and

Table 2. The mechanical system parameters

System																					
The motor	Operating configuration																				
	<table border="1"> <thead> <tr> <th>Frequency (Hz)</th> <th>Power</th> <th>Connection</th> <th>Speed (tr/mn)</th> <th>Poles</th> </tr> </thead> <tbody> <tr> <td>50</td> <td>15 kW</td> <td>Triangle connected</td> <td>1460</td> <td>4</td> </tr> </tbody> </table>	Frequency (Hz)	Power	Connection	Speed (tr/mn)	Poles	50	15 kW	Triangle connected	1460	4										
Frequency (Hz)	Power	Connection	Speed (tr/mn)	Poles																	
50	15 kW	Triangle connected	1460	4																	
The gearbox	Component																				
	<table border="1"> <thead> <tr> <th></th> <th>Carrier</th> <th>Planet</th> <th>Ring</th> <th>Sun</th> </tr> </thead> <tbody> <tr> <td>Number</td> <td>1</td> <td>3</td> <td>1</td> <td>1</td> </tr> <tr> <td>Teeth number</td> <td>—</td> <td>24</td> <td>65</td> <td>16</td> </tr> <tr> <td>Mass (kg)</td> <td>3.65</td> <td>1.22</td> <td>28.1</td> <td>0.49</td> </tr> </tbody> </table>		Carrier	Planet	Ring	Sun	Number	1	3	1	1	Teeth number	—	24	65	16	Mass (kg)	3.65	1.22	28.1	0.49
		Carrier	Planet	Ring	Sun																
	Number	1	3	1	1																
Teeth number	—	24	65	16																	
Mass (kg)	3.65	1.22	28.1	0.49																	

magnetic flux), the displacement of each component of planetary gears and its velocity. This state vector is deduced from the need of combining a first order differential system from the electrical equation and the motion equation from the mechanical system, as presented by $Z(t)$.

$$\frac{dZ(t)}{dt} = A(t, Z(t))Z(t) + B(t), \tag{16}$$

where

$$\{Z(t)\} = \{X(t) \ Y(t) \ \dot{Y}(t)\}^T. \tag{17}$$

$A(t)$ and $B(t)$ are developed in the expression below.

$$\frac{d}{dt} \begin{Bmatrix} i_{ds} \\ i_{qs} \\ \psi_{dr} \\ \psi_{dr} \\ u_1 \\ \dots \\ \dots \\ u_{12} \\ \dot{u}_1 \\ \dots \\ \dots \\ \dot{u}_{12} \end{Bmatrix} = \begin{bmatrix} e_{11} & e_{12}\omega_s & e_{13} & e_{14}(\dot{\theta}_1) & 0 & \dots & \dots & 0 & 0 & \dots & \dots & 0 \\ e_{21}\omega_s & e_{22} & e_{23}(\dot{\theta}_1) & e_{24} & 0 & \dots & \dots & 0 & 0 & \dots & \dots & 0 \\ e_{31} & 0 & e_{31} & e_{34}\omega_r & 0 & \dots & \dots & 0 & 0 & \dots & \dots & 0 \\ 0 & e_{42} & e_{43}\omega_r & e_{44} & 0 & \dots & \dots & 0 & 0 & \dots & \dots & 0 \\ 0 & 0 & 0 & 0 & 0 & \dots & \dots & 0 & 1 & \dots & \dots & 0 \\ \dots & \dots & \dots & \dots & \dots & \dots & \dots & 0 & \dots & 1 & \dots & \dots \\ \dots & \dots & \dots & \dots & \dots & \dots & \dots & 0 & \dots & \dots & \dots & 0 \\ 0 & 0 & 0 & 0 & 0 & \dots & \dots & 0 & 0 & \dots & \dots & 1 \end{bmatrix} \begin{Bmatrix} i_{ds} \\ i_{qs} \\ \psi_{dr} \\ \psi_{dr} \\ u_1 \\ \dots \\ \dots \\ u_{12} \\ \dot{u}_1 \\ \dots \\ \dots \\ \dot{u}_{12} \end{Bmatrix} + \begin{Bmatrix} \frac{v_{ds}}{\sigma L_s} \\ \frac{v_{qs}}{\sigma L_s} \\ \frac{\sigma L_s}{\sigma L_s} \\ 0 \\ \dots \\ \dots \\ 0 \\ \dots \\ \dots \\ \dots \\ \dots \\ \text{inv}(M)F_{\text{imp}} \end{Bmatrix}. \tag{18}$$

The electromechanical interaction between the motor and the gearboxes system is ensured though

- The impact of the system’s vibrations and any anomaly is presented in (18) by $\dot{\theta}_{\text{sun}}$.
- The mechanical torque transmitted to the gearbox given by the following expression

$$C_{em} = \frac{pL_m}{L_r} (\psi_{dr} i_{qs} - \psi_{qr} i_{ds}). \tag{19}$$

$\{F\}$, is given by (19), expresses the coupling terms between the electrical model and the mechanical model, which expresses the electromagnetic torque. While, $\{F_{\text{imp}}\}$, expresses the presence of any external efforts.

3. The experimental testbench

The most important step in the numerical approaches is giving credibility to results by validating them using experimental measurements. Thereby, the study presented in this paper will probe into an experimental rig as shown in the Figure 3. This testbench is composed of two parts, the

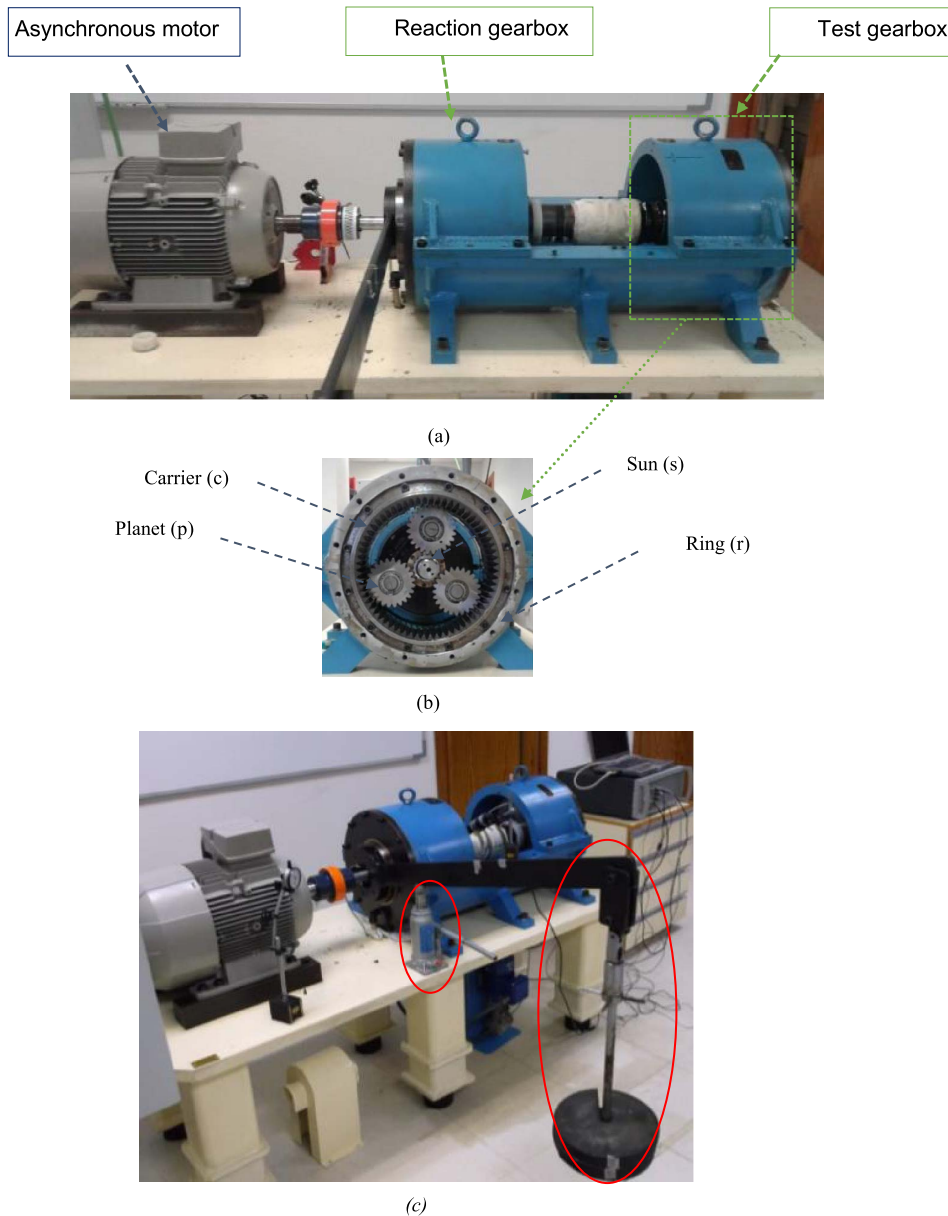


Figure 3. (a) The test bench, (b) the test gearbox, (c) the external load.

characteristics of which are illustrated in Table 2. The driving part is a three-phased asynchronous motor controlled by a Siemens inverter. The mechanical part is structured as a back-to-back planetary gearbox, which is basically composed of two stages of identical planetary gearbox (reaction and test).

Each stage, as shown in the same Figure 3, is composed of an external ring, three planets fixed on a carrier, and a sun, which is the input gear. The configuration of the bench is compacted with a mechanical power circulation for economic energy efficiency. Both gearboxes are connected to each other through a rigid hollow shaft that holds both carriers and a second one that connects the sun of the reaction gearbox to the test sun [30].

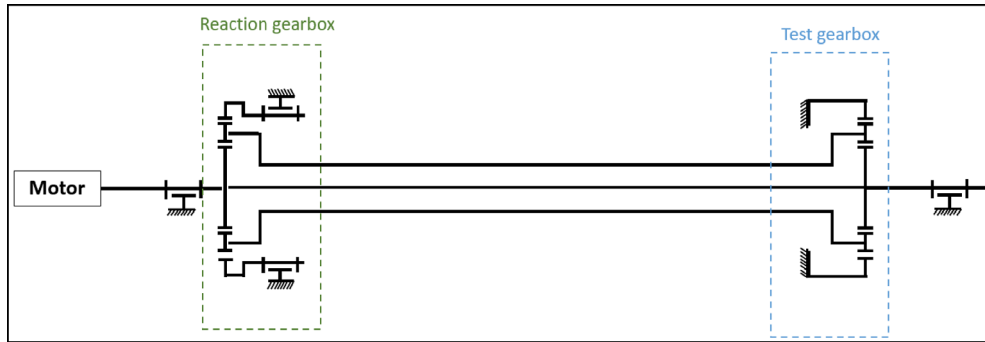


Figure 4. Back-to-back configuration in the testbench used.



Figure 5. The electric clamp.

The experimental measurements were done for constant speed fixed by fixing the motor input frequency maintained in the experiments at 20 Hz (corresponds to 570 rpm: rotating speed).

The configuration of the used test bench is compact with purely mechanical power circulation. For the mechanical power circulation type, input and output shafts of both gearboxes with identical gear ratios are connected to each other by intermediate shafts and gearboxes.

The sun gears of both planetary gear sets are connected through a common shaft and the carriers of both planetary gear sets are connected to each other through a rigid hollow shaft. This system builds a closed loop as seen in Figure 4 below.

Moreover, the design of the test bench allows applying external load on the testbench by an arm connected to the reaction gearbox. The load added on the test bench is described by external masses or by using a jark as seen in Figure 3(c).

In the experiments, we used 600 N·m load applied.

As for the instrumentations, clamp metre of type fluke i200s AC current clamp, sensitivity of 10 mV/A as shown in Figure 5 was mounted around the input wires of the motor to measure the current in each phase of the motor. The clamp was connected to a data acquisition system “LMS SCADAS 316”, controlled by LMS Test Lab, where all the data was registered and archived.

In order to highlight the sensitivity of the numerical model, to detect the tooth defect, we had introduced on one of the planets a groove as shown in Figure 6. The cut was done on the length of the teeth, with a depth and a width which equals, respectively, to 0.2 mm and 0.3 mm.

4. Numerical simulations

In order to adopt the numerical model developed in Section 2 to the test bench in Section 3, we consider a double-stage planetary gears as show in Figure 7. The mesh stiffness of the global



Figure 6. The planet defect.

system is given by $K(t) = \text{diag}(K_t, K_r)$, where t describes the test gear set and r the reaction set. For the stiffness, connections between both gearboxes were simulated to linear springs in the K_c coupling stiffness matrix. As indicated above, the connection between the test gearbox and the reaction gearbox is done through two shafts and this connection is assured in the numerical model by the matrix below.

As seen, Figure 7 illustrates a numerical schema of the test bench and clarify the connection matrix (20) between both gearboxes and all the corresponding parameters are presented in detail in Table 3. The connecting shafts are modelled by torsional stiffness K_s and K_c , where K_s is given to the stiffness of the shaft connecting the suns and K_c for the hollow shaft connecting carriers. For this testbench the reaction ring is considered free, its torsional stiffness K_{rru} equals to zero, although, the test ring is not completely clamped so a high torsional stiffness K_{rtu} is given.

$$K_c = \begin{bmatrix} k_c & 0 & 0 & 0 & 0 & -k_c & 0 & 0 & 0 & 0 \\ 0 & k_{rtu} & 0 & 0 & 0 & 0 & 0 & 0 & 0 & 0 \\ 0 & 0 & k_s & 0 & 0 & 0 & 0 & -k_s & 0 & 0 \\ 0 & 0 & 0 & 0 & 0 & 0 & 0 & 0 & 0 & 0 \\ 0 & 0 & 0 & 0 & 0 & 0 & 0 & 0 & 0 & 0 \\ 0 & 0 & 0 & 0 & 0 & 0 & 0 & 0 & 0 & 0 \\ -k_c & 0 & 0 & 0 & 0 & k_c & 0 & 0 & 0 & 0 \\ 0 & 0 & 0 & 0 & 0 & 0 & k_{rtu} & 0 & 0 & 0 \\ 0 & 0 & 0 & 0 & 0 & 0 & 0 & k_s & 0 & 0 \\ 0 & 0 & -k_s & 0 & 0 & 0 & 0 & 0 & 0 & 0 \\ 0 & 0 & 0 & 0 & 0 & 0 & 0 & 0 & 0 & 0 \\ 0 & 0 & 0 & 0 & 0 & 0 & 0 & 0 & 0 & 0 \end{bmatrix}. \quad (20)$$

In order to highlight the sensitivity of the model used to different perturbations, some tooth defects would be introduced in the coming work. Chaari *et al.* [1] had proved that the presence of

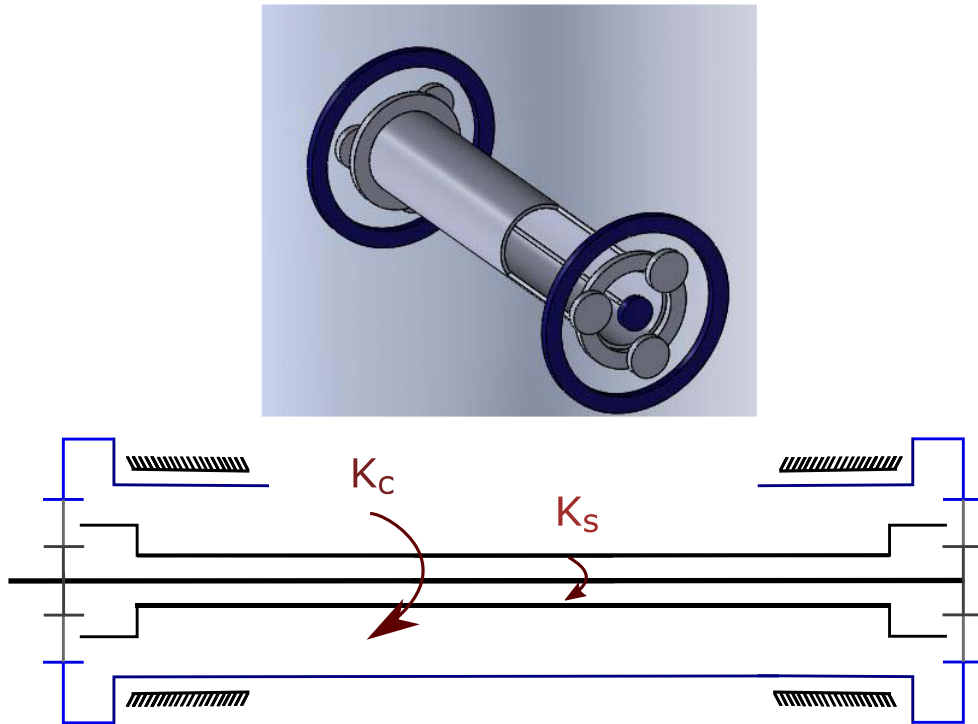


Figure 7. Numerical model of the test bench.

Table 3. The simulations parameters

Input frequency	50 Hz			
	Sun	Planet	Ring	Carrier
Moment of inertia ($\text{kg}\cdot\text{m}^2$)	352×10^{-6}	2045×10^{-6}	697767×10^{-6}	21502×10^{-6}
Reaction gearbox: torsional stiffness ($\text{N}\cdot\text{m}/\text{rad}$)			3×10^8	
Test gearbox: torsional stiffness ($\text{N}\cdot\text{m}/\text{rad}$)			0	
Shaft stiffness ($\text{N}\cdot\text{m}/\text{rad}$)	9.3×10^7	—	—	3.7×10^8

a breakage generates a decrease in the meshing stiffness the moment the defected gear meshes with another pair of teeth. This fluctuation is relatively due to the decrease of the contact area while meshing the defected tooth.

For the healthy configuration, Figure 8(a) illustrates the temporal evolution of the gear mesh stiffness, ensuring the contact between planet–sun (the blue diagram) and the meshing stiffness, ensuring the contact between planet–ring (the green diagram). Several authors like Chaari *et al.*; Merainani *et al.* [1, 31] had proved that the presence of a tooth defect is seen in the gear meshing stiffness through a decrease in its amplitude each time the defected tooth gets involved in a contact, once per revolution of the damaged gear.

To study the sensitivity of the electromechanical approach suggested in investigating the dynamic behaviour of the mechanical system, we assumed the presence of tooth breakage that resulted in a decrease in the corresponding gear mesh stiffness per revolution of the defected gear

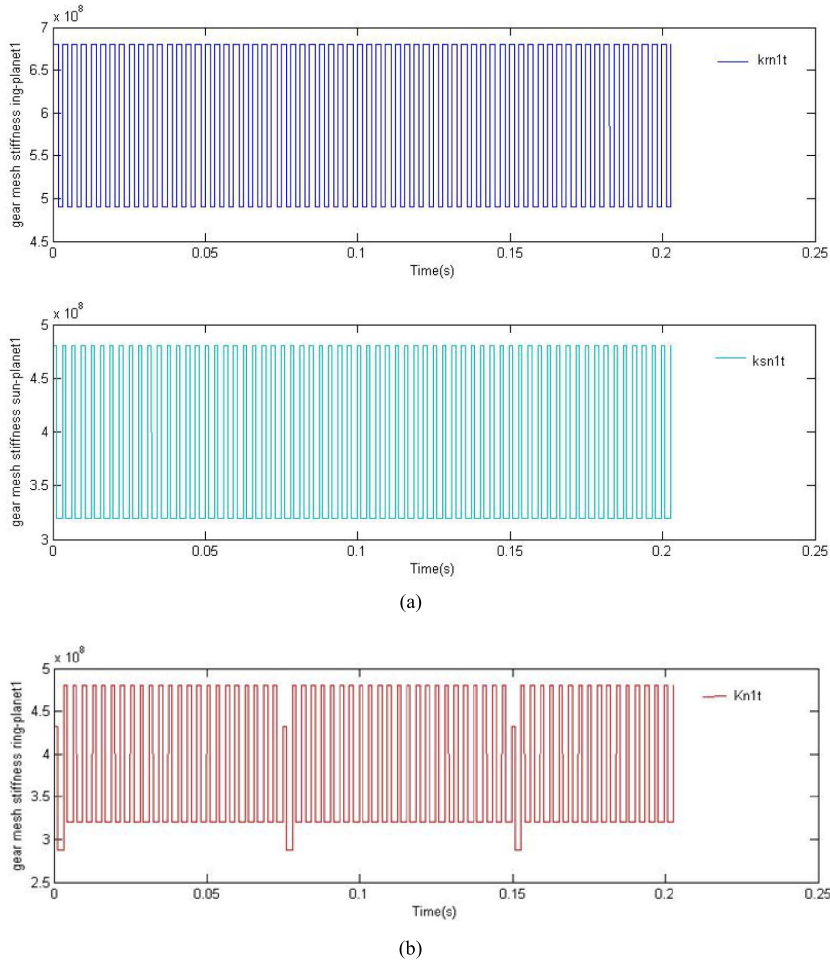


Figure 8. The gear meshing stiffness. (a) The gear meshing stiffness for the healthy configuration (blue: ring–planet1) (green: sun–planet1); (b) the impact of the tooth defect on the gear meshing stiffness.

as seen in Figure 8(b). The objective beyond this paper is to highlight the sensitivity of the stator current to the mechanical anomalies. Consequently, different defects were tested in the coming studies by modifying the placement and the number of defects.

The resolution of the system (18) has been done by using the Runge–Kutta method due to the appearance of nonlinear terms in the torque expression. The time step calculation is taken depending on the mechanical parameter, and in order to simplify the calculation, the time increment is given by $T_{\text{incr}} = T_{\text{eng}}/300$, where T_{eng} is the gear mesh frequency.

5. Results and discuss

5.1. Numerical simulations in time domain

The direct-quadrature-zero transformation is a mathematical transformation used to simplify the analysis of a three-phased motor. This method uses the three phases current presented in a sinusoidal signal to obtain a constant current involving different electrical parameters [29].

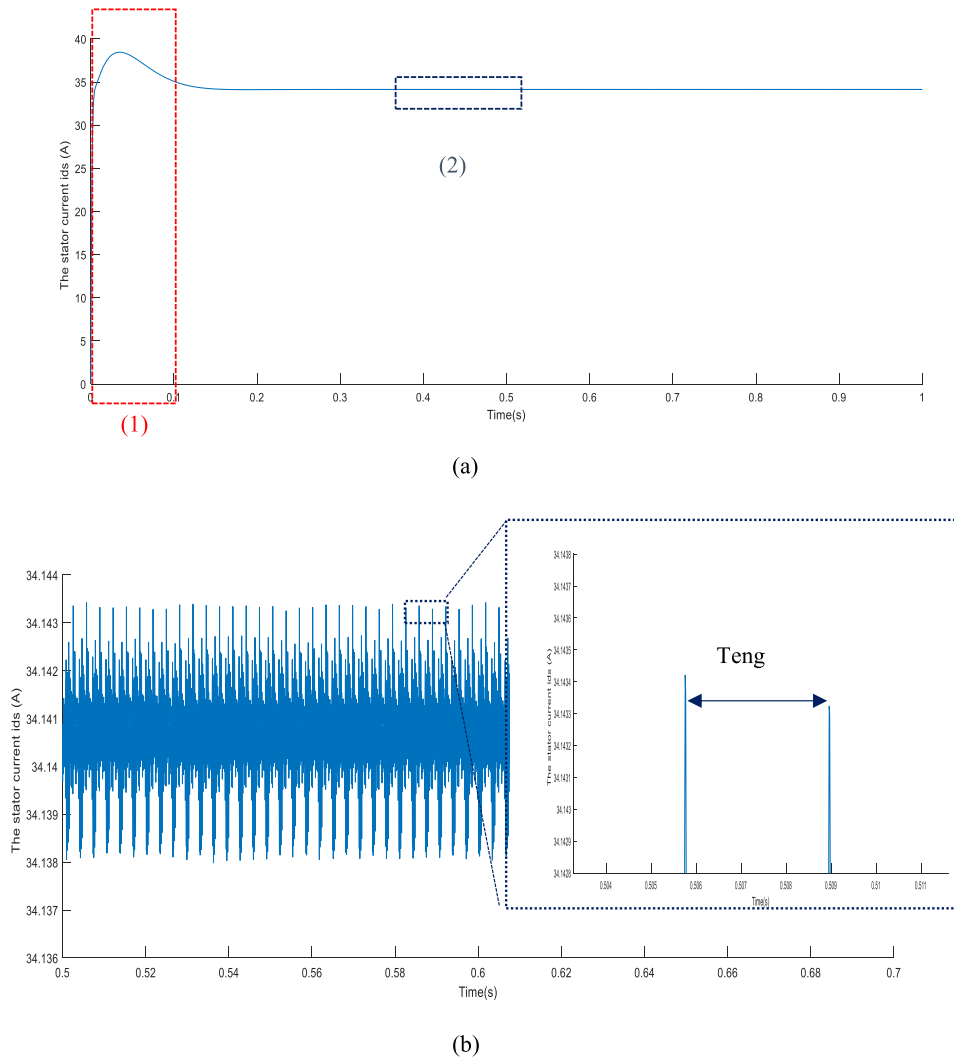


Figure 9. Current signal for healthy configuration. (a) The current temporal signal; (b) zoom in on the zone (2).

Table 4. Key frequencies

	Notation	Expression	Value (Hz)
Sun frequency (input)	f_s	$f_s = \frac{N}{60}$	24.33
Carrier frequency (output)	f_c	$f_c = \frac{z_s}{(z_r + z_s)} f_s$	4.80
Gear meshing frequency	F_m	$F_m = z_r f_c$	312.47

In this context, this approach’s objective is to investigate the electromechanical interaction between the driving machine and the mechanical system.

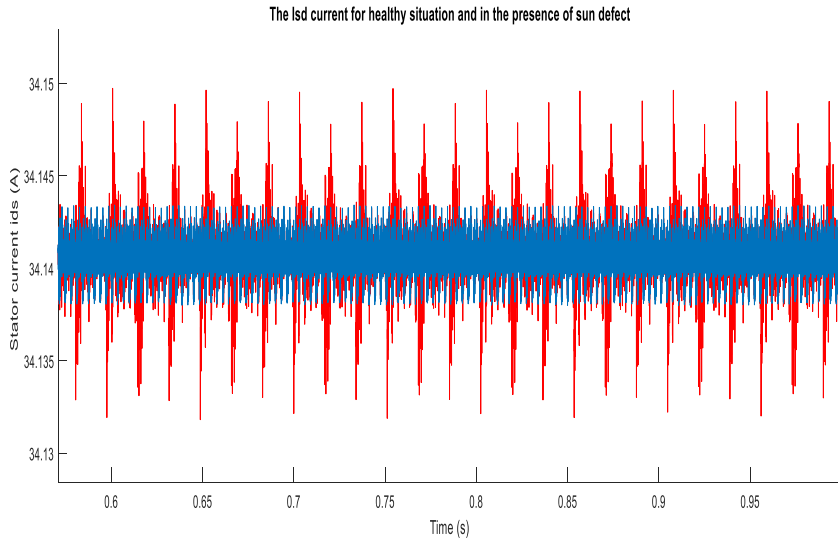


Figure 10. Stator current signal for healthy gears (blue) and in the presence of sun defect (red).

Figure 9 illustrates the temporal evolution of the stator current i_{ds} obtained from the Park transformation. The current signal is divided into two parts. The steady state, which is the concern of this study, and the transitional regime that represents the run up of the motor. For this approach only results seen in the steady state are representative. Therefore, in the rest of the paper, we are interested in that part of the signal. In Figure 5(b) the current signal represents a periodic fluctuation with an amplitude 5×10^{-3} and a period that corresponds to the gear mesh period T_{eng} given by

$$T_{eng} = \frac{1}{F_m}, \quad (21)$$

where F_m is the gear meshing frequency, given in Table 4.

The appearance of the meshing frequency in the current i_{ds} is explained mathematically by the transmission of the sun velocity's signal seen in (18). On the other hand, the meshing phenomena is transmitted to the motor as a load fluctuation which will affect the speed of the shaft and produce vibrations each time the planet accomplishes one relative revolution. Hence, the simulated stator current obtained by the equivalent circuit is sensitive to the electromechanical interaction between the asynchronous motor and the gearboxes.

5.2. Damaged gearbox

5.2.1. Sun defect

Generally, the sun of the planetary gearbox is considered the first part attacked by tooth defects. The pitting process starts with a fatigue crack that initiates most of the time at the surface. When the crack grows, the surface loses a piece of material which results in a pit. This loss of material leads to the loss of contacts between the meshing teeth, and there on have impacts on the gear meshing frequency. Therefore, we consider the presence of a local defect on one of the sun teeth. When the defected tooth meshes with one of the planets, the vibration signals are modulated by impulse signals. These impulsions are justified by revolutionary phenomena that repeats each time the defected tooth is in contact with one planet. Therefore, Figure 10 presents

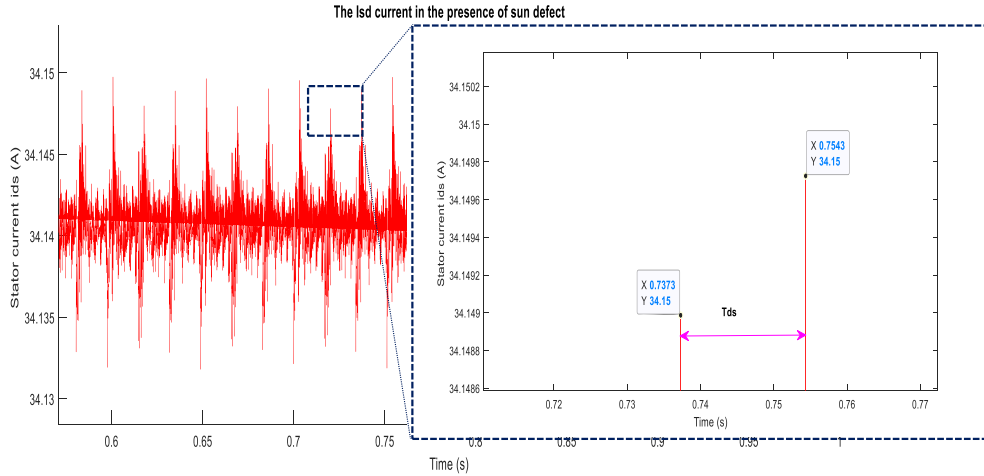


Figure 11. The impact of the sun tooth defect on the stator current i_{ds} .

the current signal in the defect’s presence comparing with the healthy configuration. The sun tooth defect impacts the signal three times along the revolution of the sun due to the contact with three planets. Thus, the vibration signals impacts presented in the mechanical system were transmitted to the motor by the sun shaft and seen in the stator current signals.

Besides the fluctuation seen in the current signal due to the gear meshing, Figure 11 clearly shows the appearance of the variation of the stator current i_{ds} in the presence of sun tooth defect. The temporal variation shows current modulation by T_{ds} given by

$$T_{ds} = \frac{1}{F_{ds}} \tag{22}$$

$$F_{ds} = N(f_s - f_c) = \frac{Nz_r}{z_r + z_s} f_s \tag{23}$$

where f_s is the sun frequency and f_c is the carrier frequency as demonstrated in Table 4.

The increase of the current amplitude when the defected tooth gets in contact each time is totally foreseen. Meshing defected tooth generate additional load which makes the system is partially overloaded.

5.2.2. Planet defect

The impact of the planet defect on the signal depends on its localization, therefore, in this case we assumed two different cases: The defect is present in one side of the planet or it is present in both sides.

The defected side of the damaged tooth that gets in contact with the sun presents a modulation in the recorded signals once each revolution of the planet (T_{dp}) as it is illustrated in Figure 12(a). So, the defect on the planet would be seen by its frequency given by

$$T_{dp} = \frac{1}{F_{dp}} \tag{24}$$

$$F_{dp} = \frac{F_m}{z_p} = \frac{z_s z_r}{z_p(z_r + z_s)} f_s. \tag{25}$$

We assume that the same defect is applied from both sides of the same tooth. When the sun is in contact with surface A, this contact will produce a modulation in the current signals as it was explained in the case of a tooth defect from one side so that the defect A will appear in each F_{dp} [6].

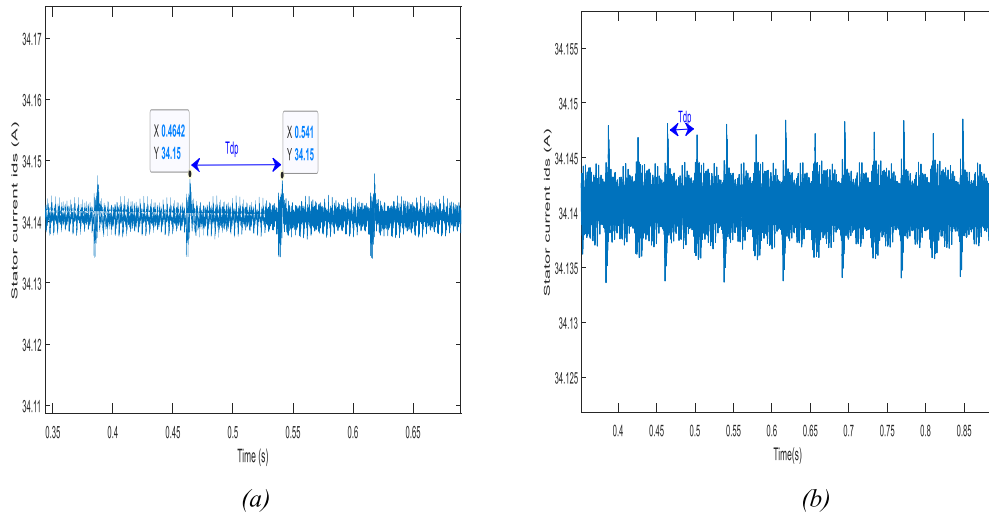


Figure 12. i_{ds} current signal in the presence of planet defect. (a) Defect on one side of the tooth, (b) defect on both sides of the tooth.

After a half revolution of the planet, the defected tooth will be in contact with the ring tooth but with the surface B this time, which will be seen itself in the current spectrum by the same frequency. Although both defects will not be seen in the same amplitude as it is shown in Figure 10(b), in one revolution of the planet the tooth defect is signed twice as it is given by

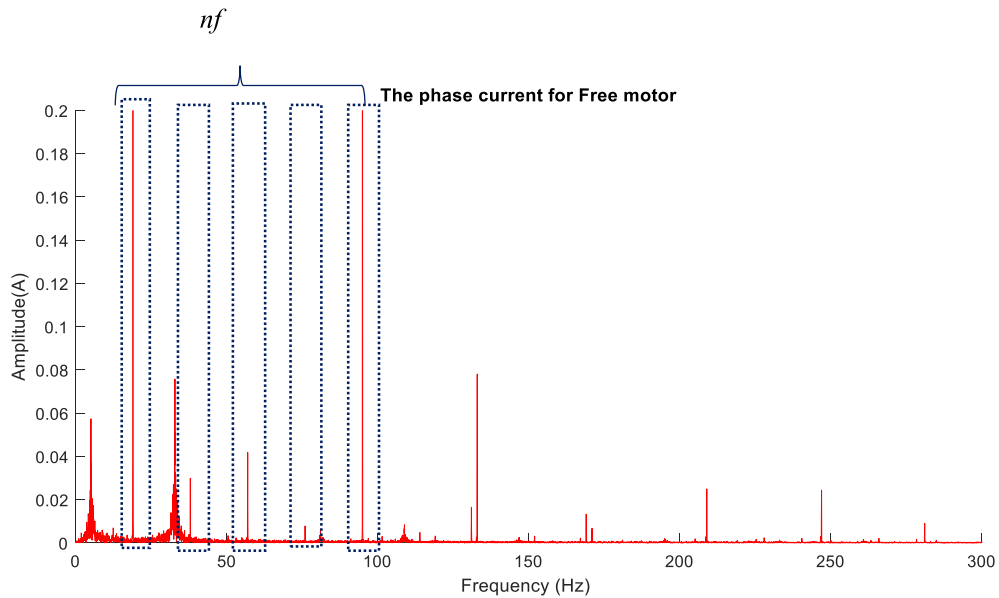
$$F_{dp} = 2 \frac{F_m}{z_p} = 2 \frac{z_s z_r}{z_p(z_r + z_s)} f_s. \quad (26)$$

5.3. Experimental validations

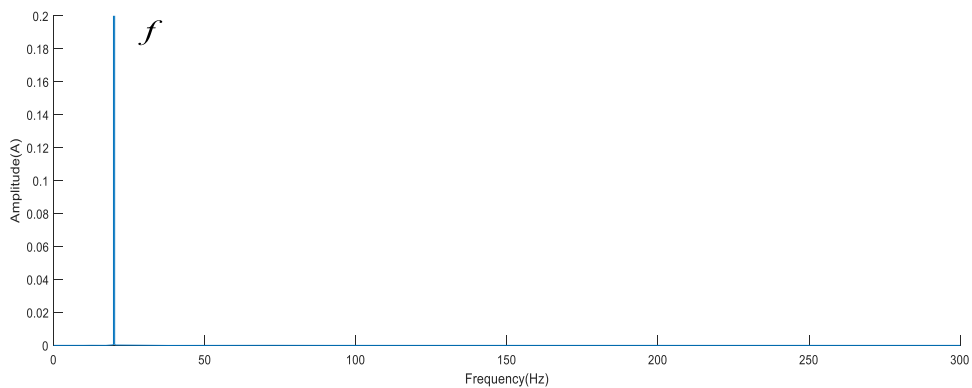
In order to validate the results, obtained by the numerical simulations, some experimental measurements will be presented. The system was running at 570 rpm, the electrical frequency of the motor was maintained at 20 Hz. First, we noticed some differences between the experimental and numerical measurements. These differences are mainly related to the state of the motor as seen in Figure 13(a) and excluded from the simulations since the machine was considered perfect due to several simplifications adopted in the modelling to reduce the system complexity.

For the numerical model, the motor is not supposed to present any behavioural imperfections, then delivering a perfect sinusoidal current. Therefore, the frequency spectrum of the phase current is dominated only by the electrical frequency as seen in the Figure 13(b). Although in reality, as seen in Figure 12(a), many harmonics also appear. These harmonics are signed in the presence of the mechanical or electrical anomalies in the motor [32]. The objective of this part of the paper is to highlight the sensitivity of the model to the electromechanical interaction and the detection of the appearance of any tooth defect. For the healthy configuration, we applied the fast Fourier transformation on the temporal signal seen in Figure 7(b) to obtain the frequency spectrum. Clearer Figure 14 shows that the current spectrum i_{ds} is dominated by the gear meshing frequency and its harmonics.

In order to obtain the current in the phase of the motor, we used the inverse of the Park transformation. The Figure 14 illustrates the phase current frequency spectrum, which is dominated by the electrical frequency given as 20 Hz in these simulations. Therefore, in order to highlight the frequency with low amplitude, we used the Hanning window to plot the coming simulations results for the phase current. Besides, in the same figure, we notice the appearance of the additional



(a)



(b)

Figure 13. Phase current for free motor. (a) Experimental measurements; (b) numerical simulations.

peaks related to the meshing frequency, which is given by the expression

$$|f \pm nf_{\text{mesh}}|, \quad (27)$$

where $n \in \mathbb{N}^*$, $f_{\text{mesh}} = 121.9$ Hz.

In reality the torque oscillations can exist even in the healthy case because of space and time harmonics, this is what explains its appearance in the spectrum of the phase current measured and showed in Figure 16.

In this study, the experiments were done to prove the sensitivity of the motor current to investigate the dynamic behaviour of the mechanical system, also to justify the results obtained in the simulations. Like results in Figure 15, the load torque oscillations due to the gear meshing

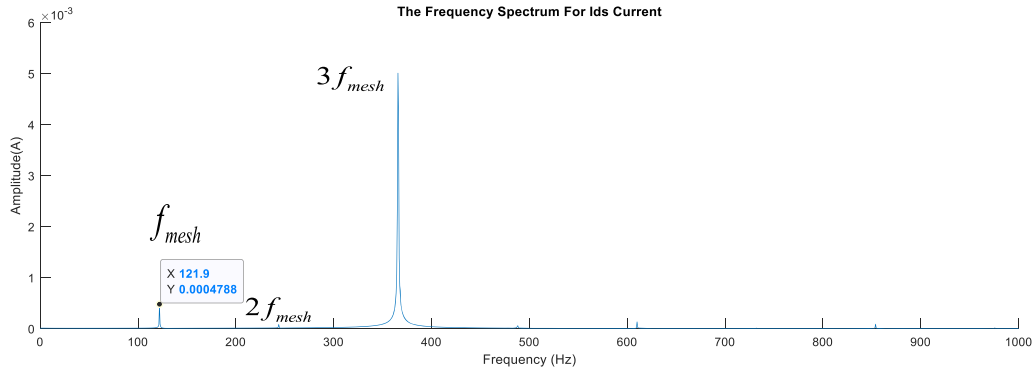


Figure 14. The frequency spectrum of the i_{ds} current in the HEALTHY configuration.

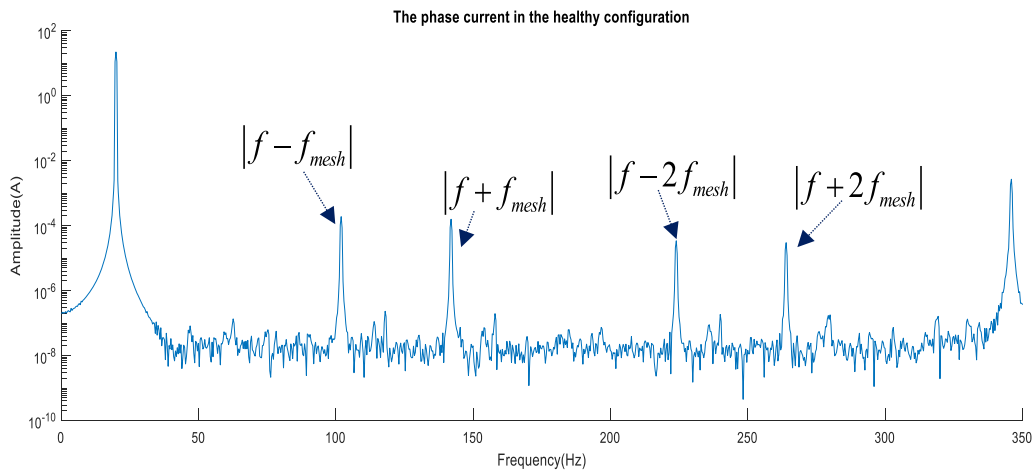


Figure 15. The frequency spectrum of a phase current in the HEALTHY configuration (numerical simulations).

phenomena is modulating the input motor current and appear in the spectrum as additional frequencies given by (27).

5.3.1. Planet defect

Besides the appearance of the gear meshing frequency and its harmonics, Figure 17 illustrates the appearance of additional frequencies, due to the defect included on the defect in the frequency spectrum of the i_{ds} current.

Thomson had shown in [33] that the appearance of a defect in the mechanical system produces a load fluctuation, which causes some speed oscillations that modulate the current input. In that regard, Figure 18 presents the phase current obtained from the current shown above. In fact, the vibrations produced by a defect of a mechanical component acts on the induction machine as a torque ripple $\Delta T_i(t)$ which would produce a speed ripple $\Delta\omega_i(t)$.

Hence, the consequent mechanical angular variation will generate an angular fluctuation in the magnetic flux of the device and since the induction machines are considered symmetrical systems because of the magnetic rotating field, the appearance of any anomaly will impact the symmetrical properties [34]. The planet defect affects the phase current by modulating

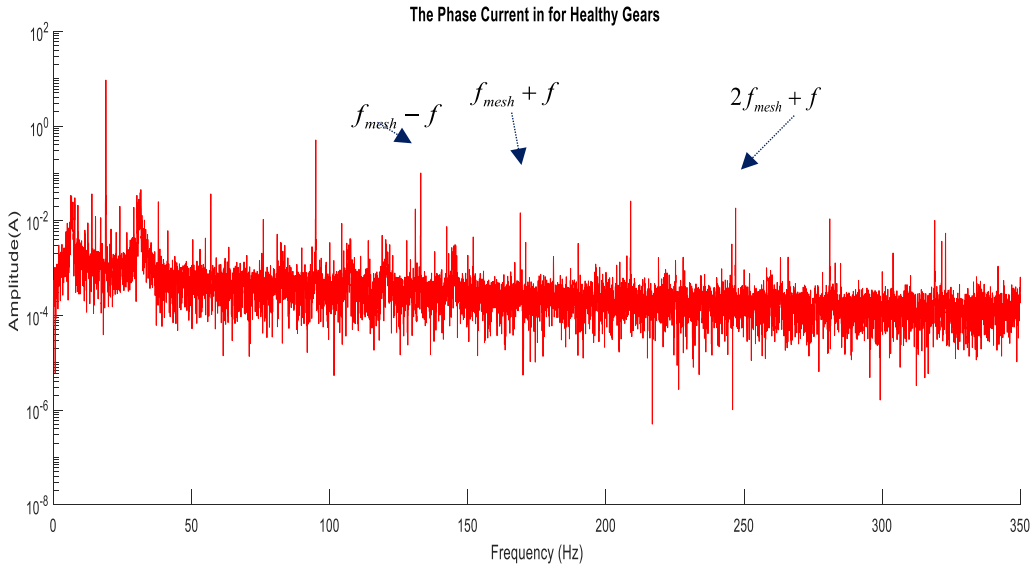


Figure 16. The frequency spectrum of a phase current (experimental results).

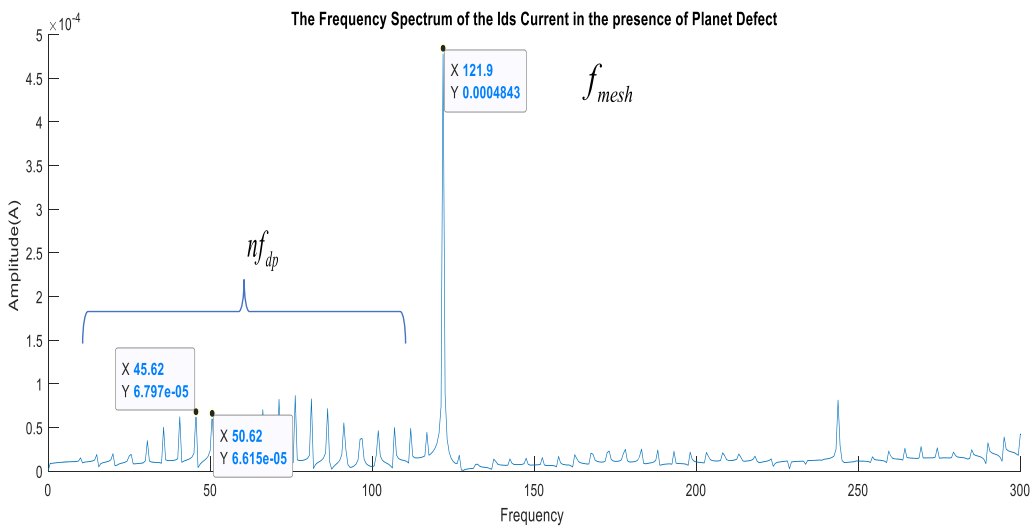


Figure 17. The frequency spectrum of the ids current in the presence of planet defect.

the electric frequency. Therefore, we justify the appearance of the related defect frequency modulated by the supply frequency (28) and modulated by the mesh frequency

$$|f \pm nf_{dp}| \tag{28}$$

$$|f \pm nf_{dp} \pm mf_{mesh}|. \tag{29}$$

The presence of the related frequencies to the planet defect are justified in the phase current signal measured on the test bench. Figure 19 highlights the presence of sidebands that corresponds to those seen in Figure 18 given by (28). The experimental measurements justify the

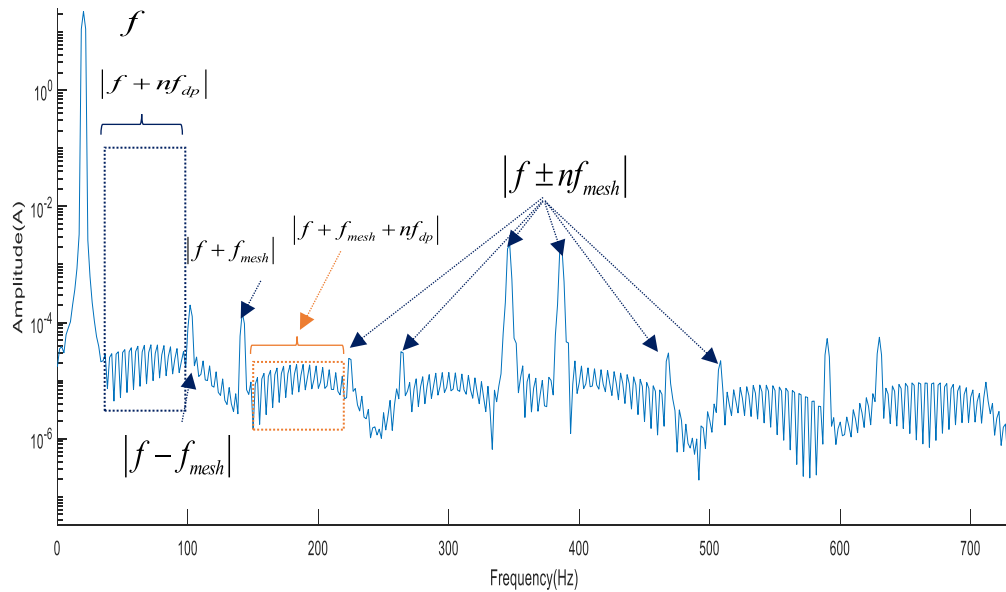


Figure 18. The frequency spectrum of the phase current in the presence of planet defect (numerical simulations).

results obtained by the simulations. Although, the simplification adopted, the numerical model is sensitive to the teeth contact and to the tooth defects.

6. Conclusion

Using MCSA, this paper had presented a deep overview of the impact of tooth defects on the start current by numerical simulations and experimental measurements. The approach used in modelling, was based on an electromechanical system that defines the interaction between asynchronous machine and double-stage planetary gearboxes. The numerical model was obtained in three main stages: a first part that had described the dynamic model of the asynchronous motor. For the electrical part, a three-phased machine was described by an equivalent bi-phased circuit obtained by the Park transformation which involves all the physical parameters.

The second part consisted of dynamic modelling of a double stage's gearboxes. In the model used, only the torsional degree of freedom was considered for simplification purposes. And finally, a global model based on the electromechanical torque transmitted from the motor to the mechanical system and on the dynamic response of the gearboxes propagated back to the motor. Numerical results obtained in stationary operating conditions had highlighted the visibility of the impact of the mechanical system on the electrical model. It was clearly seen in the appearance of the gear meshing frequency in the frequency spectrum of the Ids current. Also, in the case of the teeth defect, the electrical model was sensitive to detect the appearance of an anomaly in the mechanical system. Comparing the obtained results from the numerical simulations to the experimental measurements, the mechanical frequencies were related to the electrical frequency that dominates the phase frequency spectrum.

In the future, the electrical model will be extended rising its complexity to be closer to the real system by including the imperfections in the electric machine. This technique would be a

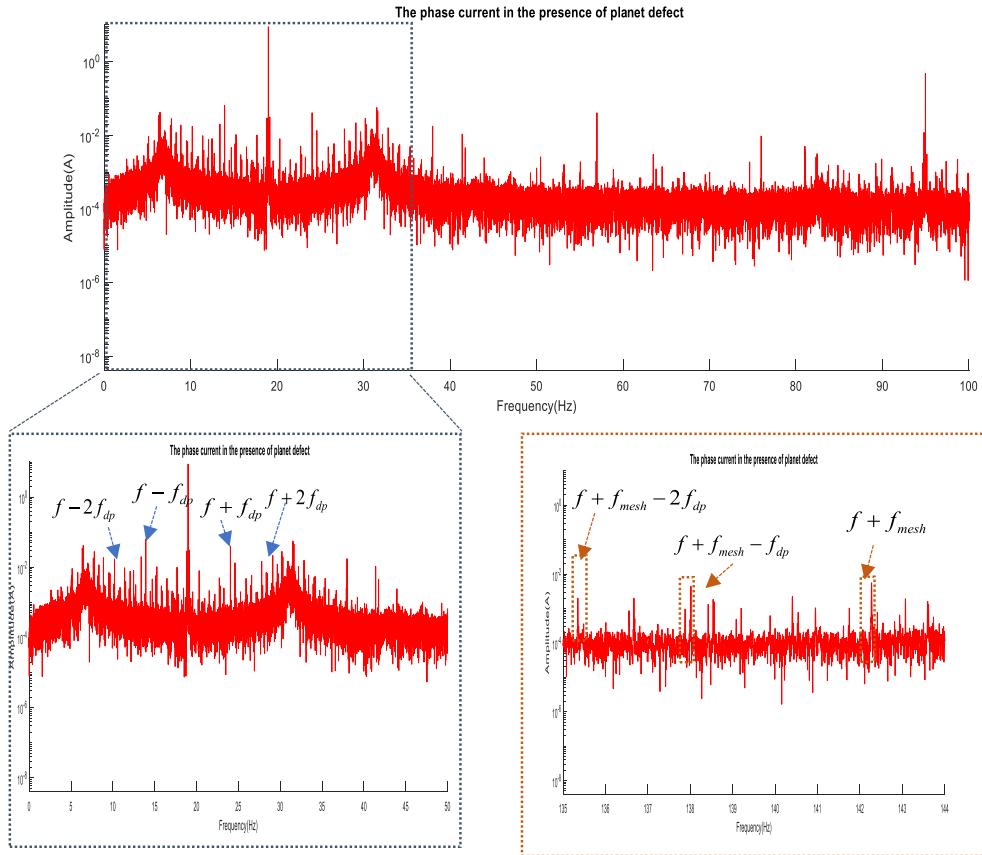


Figure 19. The frequency spectrum of the phase current in the presence of planet defect (experimental measurements).

leading method in diagnosing the rotating system due to its accuracy, and mainly its accessibility, in different operating conditions.

Nomenclature

Electrical system

- r Subscripts for the rotor
- s Subscripts for the stator
- j Subscripts for the motor phase, where $j \in \{a, b, c\}$
- R Subscripts for the resistance
- L Subscripts for the self-inductance
- M Subscripts for the mutual inductance
- i Subscripts for the current
- v Subscripts for the voltage
- ψ Subscripts for the magnetic flux
- ω Subscripts for the angular velocity
- f Subscripts for the motor frequency
- N Subscripts for the motor speed (rpm)
- p Subscripts for the number of pairs of poles

Mechanical system

s	Subscripts for the sun gear
r	Subscripts for the ring gear
n_i	Subscripts for the planet gear ($i = 1 : 3$)
c	Subscripts for the carrier gear
t	Subscripts for the test gearbox
r	Subscripts for the reaction gearbox
f_i	Subscripts for the frequency of the i th gear, where $i \in \{s, r, c, 1, 2, 3\}$
k	Subscripts for the stiffness
M	Subscripts for the mass
C	Subscripts for the damping
C_{em}	Subscripts for the electromechanical torque

Acknowledgements

The authors would like to acknowledge the help provided by the project “Dynamic behaviour of gear transmissions in nonstationary conditions”, ref. DPI2017-85390-P, funded by the Spanish Ministry of Science and Technology.

They would like to thank the University of Cantabria cooperation project for the doctoral training to Sfax University students.

References

- [1] F. Chaari, R. Zimroz, W. Bartelmus, T. Fakhfakh, M. Haddar, “Modeling of local damages in spur gears and effects on dynamics response in presence of varying load conditions”, *Proc. Surveill.* **6** (2011), p. 1-19.
- [2] F. Chaari, T. Fakhfakh, M. Haddar, “Dynamic analysis of a planetary gear failure caused by tooth pitting and cracking”, *J. Fail. Anal. Prev.* **6** (2006), no. 2, p. 73-78.
- [3] A. Fernandez del Rincon, F. Viadero, M. Iglesias, A. de Juan, P. Garcia, R. Sancibrian, “Effect of cracks and pitting defects on gear meshing”, *Proc. Inst. Mech. Eng., Part C: J. Mech. Eng. Sci.* **226** (2012), no. 11, p. 2805-2815.
- [4] A. Fernandez-del Rincon, P. Garcia, A. Diez-Ibarbia, A. De-Juan, M. Iglesias, F. Viadero, “Enhanced model of gear transmission dynamics for condition monitoring applications: effects of torque, friction and bearing clearance”, *Mech. Syst. Signal Process.* **85** (2017), p. 445-467.
- [5] B. Li, X. Zhang, J. Wu, “New procedure for gear fault detection and diagnosis using instantaneous angular speed”, *Mech. Syst. Signal Process.* **85** (2017), p. 415-428.
- [6] Y. Gui, Q. K. Han, Z. Li, F. L. Chu, “Detection and localization of tooth breakage fault on wind turbine planetary gear system considering gear manufacturing errors”, *Shock Vib.* **2014** (2014), article no. 692347.
- [7] Q. Miao, Q. H. Zhou, “Planetary gearbox vibration signal characteristics analysis and fault diagnosis”, *Shock Vib.* **2015** (2015), article no. 126489.
- [8] C. Zhang, S. Wang, G. Bai, “An accelerated life test model for solid lubricated bearings based on dependence analysis and proportional hazard effect”, *Acta Astronaut.* **95** (2014), p. 30-36.
- [9] M. Attar, “A transfer matrix method for free vibration analysis and crack identification of stepped beams with multiple edge cracks and different boundary conditions”, *Int. J. Mech. Sci.* **57** (2012), no. 1, p. 19-33.
- [10] X. Jiang, S. Li, Q. Wang, “A study on defect identification of planetary gearbox under large speed oscillation”, *Math. Probl. Eng.* **2016** (2016), article no. 5289698.
- [11] C. Kar, A. R. Mohanty, “Monitoring gear vibrations through motor current signature analysis and wavelet transform”, *Mech. Syst. Signal Process.* **20** (2006), no. 1, p. 158-187.
- [12] Y. Yi, D. Qin, C. Liu, “Investigation of electromechanical coupling vibration characteristics of an electric drive multistage gear system”, *Mech. Mach. Theory* **121** (2018), p. 446-459.
- [13] H. Balan, M. I. Buzdugan, P. Karaisas, “Fault identification on electrical machines based on experimental analysis”, in *Advances in Condition Monitoring of Machinery in Non-Stationary Operations*, Springer, Berlin, Heidelberg, 2014, p. 611-630.
- [14] M. Blodt, P. Granjon, B. Raison, G. Rostaing, “Models for bearing damage detection in induction motors using stator current monitoring”, *IEEE Trans. Ind. Electron.* **55** (2008), no. 4, p. 1813-1822.

- [15] J. Zhang, J. S. Dhupia, C. J. Gajanayake, "Model based current analysis of electrical machines to detect faults in planetary gearboxes", in *2014 IEEE/ASME International Conference on Advanced Intelligent Mechatronics*, IEEE, 2014, p. 1616-1621.
- [16] S. Nandi, R. M. Bharadwaj, H. A. Toliyat, "Performance analysis of a three-phase induction motor under mixed eccentricity condition", *IEEE Trans. Energy Convers.* **17** (2002), no. 3, p. 392-399.
- [17] R. R. Schoen, T. G. Habetler, F. Kamran, R. G. Bartfield, "Motor bearing damage detection using stator current monitoring", *IEEE Trans. Ind. Appl.* **31** (1995), no. 6, p. 1274-1279.
- [18] S. H. Kia, H. Henao, G.-A. Capolino, "Gearbox monitoring using induction machine stator current analysis", in *2007 IEEE International Symposium on Diagnostics for Electric Machines, Power Electronics and Drives*, IEEE, 2007, p. 149-154.
- [19] R. Yacamini, K. S. Smith, L. Ran, "Monitoring torsional vibrations of electro-mechanical systems using stator currents", *J. Vib. Acoust.* **120** (1998), no. 1, p. 72-79.
- [20] N. Feki, G. Clerc, P. Velez, "An integrated electro-mechanical model of motor-gear units—applications to tooth fault detection by electric measurements", *Mech. Syst. Signal Process.* **29** (2012), p. 377-390.
- [21] G. Kron, "Equivalent circuits for the hunting of electrical machinery", *Trans. Amer. Inst. Electr. Eng.* **61** (1942), no. 5, p. 290-296.
- [22] J. R. Ottewill, A. Ruszczky, D. Broda, "Monitoring tooth profile faults in epicyclic gearboxes using synchronously averaged motor currents: mathematical modeling and experimental validation", *Mech. Syst. Signal Process.* **84** (2017), p. 78-99.
- [23] A. Gao, Z. Feng, M. Liang, "Permanent magnet synchronous generator stator current AM-FM model and joint signature analysis for planetary gearbox fault diagnosis", *Mech. Syst. Signal Process.* **149** (2021), article no. 107331.
- [24] D. Ramya, R. Basha, M. L. Bharathi, "Fault diagnosis of induction motor drive using motor current signature analysis", in *ICASISSET 2020, 16-17 May 2020, Chennai, India*, EAI, 2021.
- [25] J. Lin, R. G. Parker, "Analytical characterization of the unique properties of planetary gear free vibration", *J. Vib. Acoust.* **121** (1999), no. 3, p. 316-321.
- [26] M. Iglesias, A. Fernandez del Rincon, A. De-Juan, A. Diez-Ibarbia, P. Garcia, F. Viadero, "Advanced model for the calculation of meshing forces in spur gear planetary transmissions", *Meccanica* **50** (2015), no. 7, p. 1869-1894.
- [27] N. Feki, "Modélisation électro-mécanique de transmissions par engrenages: applications à la détection et au suivi des avaries", PhD Thesis, INSA, Lyon, 2012.
- [28] P. Barret, *Régimes Transitoires des Machines Tournantes Électriques*, Eyrolles, Paris, 1987, 209 pages.
- [29] A. A. Ansari, D. M. Deshpande, "Mathematical model of asynchronous machine in MATLAB Simulink", *Int. J. Eng. Sci. Technol.* **2** (2010), no. 5, p. 1260-1267.
- [30] A. Hammami, A. Fernandez Del Rincon, F. Chaari, M. I. Santamaria, F. V. Rueda, M. Haddar, "Effects of variable loading conditions on the dynamic behaviour of planetary gear with power recirculation", *Measurement* **94** (2016), p. 306-315.
- [31] B. Merainani, D. Benazzouz, C. Rahmoune, "Early detection of tooth crack damage in gearbox using empirical wavelet transform combined by Hilbert transform", *J. Vib. Control* **23** (2017), no. 10, p. 1623-1634.
- [32] D. Miljković, "Brief review of motor current signature analysis", *HDKBR Info Mag.* **5** (2015), no. 1, p. 14-26.
- [33] W. T. Thomson, "On-line current monitoring to detect electrical and mechanical faults in three-phase induction motor drives", in *Proceedings of International Conference on Life Management of Power Plants, December 1994*, IET, 1994, p. 66-73.
- [34] A. Bellini, F. Filippetti, C. Tassoni, G.-A. Capolino, "Advances in diagnostic techniques for induction machines", *IEEE Trans. Ind. Electron.* **55** (2008), no. 12, p. 4109-4126.